Journal of Materials Chemistry A

Synthesis, characterization, and photocatalytic activity of Au-ZnO nanopyramids

Journal:	*Journal of Materials Chemistry A*
Manuscript ID:	TA-ART-02-2015-001344.R1
Article Type:	Paper
Date Submitted by the Author:	28-May-2015

Complete List of Authors:	Ranasingha, Oshadha; West Virginia University, Department of Physics Wang, Congjun; URS Corporation, ; National Energy Technology Laboratory, Ohodnicki, Paul; National Energy Technology Laboratory, Lekse, Jonathan; National Energy Technology Laboratory, Lewis, James; West Virginia University, Matranga, Christopher; National Energy Technology Laboratory, Molecular Science Division

Journal Name

RSCPublishing

ARTICLE

Synthesis, characterization, and photocatalytic activity of Au-ZnO nanopyramids

Cite this: DOI: 10.1039/x0xx00000x

Oshadha K. Ranasingha,*[a,b] Congjun Wang,[b,c] Paul R. Ohodnicki, Jr.,[b] Jonathan W. Lekse,[b,c] James P. Lewis,[a,b] Christopher Matranga*[b]

Received 00th January 2012,
Accepted 00th January 2012

DOI: 10.1039/x0xx00000x

www.rsc.org/

Nanocrystalline Au-ZnO heterostructures were synthesized using a wet-chemical process where single-crystalline ZnO grows along the [0001] direction on top of polycrystalline Au seeds. High resolution transmission electron microscopy finds a 3.5% expansion of the ZnO (002) plane at the heterostructure interface. Rietveld analysis of x-ray diffraction patterns from ZnO and Au-ZnO powders find that the crystallographic microstrain in the metal oxide is 0.047% and 0.146%, respectively, illustrating that the crystallographic expansion at the heterostructure interface is detectable by bulk characterization techniques. Broad-band photo-degradation studies with methylene blue find that the Au-ZnO heterostructures decompose the dye 6 times faster than pure ZnO. Wavelength-dependent photodegradation studies illustrate direct gap excitation of the ZnO component of the heterostructure is required to initiate dye decomposition. The mechanistic details leading to this photocatalytic activity are discussed.

1.0 Introduction

Heterostructures of oxides and metals have been studied extensively over the past few decades for photocatalysis due to their enhanced catalytic activity over just the oxide material. [1-8] In fact, heterostructures of Au and ZnO are one of the most widely studied photoactive materials due to the higher charge separation efficiency and enhanced photo-catalytic activity imparted to the ZnO by the addition of Au.[3, 5, 9] As such, Au-ZnO heterostructures can be used for solar energy conversion to electricity, photodegradation of organic pollutants, and photochemical water splitting.[6, 10, 11]

Several papers in the literature describe how the size and shape of Au-ZnO heterostructures can be controlled by using different synthetic approaches.[1, 4, 8] Yao et al.[8] were able to selectively photodeposit Au particles at the tips or basal surfaces of ZnO nanoparticles with a pyramid shape. Li et al.[4] and Flomin et al.[1] used wet chemical methods to grow well-formed ZnO nanopyramides from the surfaces of Au seeds. He et. al.[3] have reported on heterogeneous powders of Au-ZnO heterostructures which have been evaluated for the photodegradation of bacteria.

All of these works find that very subtle changes in the synthetic approaches yield dramatic changes in the general morphology of Au-ZnO particles. In particular, the synthetic steps can be used to control where the Au is deposited as well as the structural details of the Au-ZnO interface. Currently, there is little understanding in the literature of how these subtle structural details impact localized changes in electronic structure near the interface, defects arising from the heterostructuring step, and the final photocatalytic activity of the heterostructure. As such, more investigations are needed to develop insight into the final chemical properties of these materials.

In this work, we have synthesized Au-ZnO heterostructures using a wet chemical method that attempts to minimize the use of organic surfactants that can block catalytically active surface sites. In this system, Au nanoparticle seeds are used to nucleate the growth of ZnO structures with a pyramidal-type structure. A previously unreported lattice expansion of ~3.5% is found for ZnO in the first ~1.5 nm of the Au-ZnO interface. Photocatalytic dye degradation studies of Au-ZnO find that direct gap excitation is required to initiate photodecomposition and that the heterostructure has significantly higher catalytic activity than pure ZnO. We provide experimental evidence that the Au nanoparticles contribute to the higher catalytic activity of Au-ZnO by widening the band gap of ZnO, improving band alignment for the injection of charge carriers into solution species, and by increasing spatial separation of photogenerated charge carriers.

2.0 Experimental section

2.1 Materials

Hydrogen tetrachloroaurate (III) hydrate ($HAuCl_4 \bullet 4H_2O$), 99.9 %, Zinc acetate dehydrate, methanol, 99.9 %, hexane, 99.9 % and acetone, 99.9 % were purchased from Alfa Aesar. Tert-butylamine borane complex, oleylamine, C18 content 80-90 % and dodecanol, 98 % were purchased from Acros Organics.

2.2 Synthesis of Au nanoparticles

Au nanoparticles were synthesized using the procedure of Peng *et al.*[12]. $HAuCl_4 \bullet 4H_2O$ (0.5 mmol) was added to a three-neck flask with the mixture of oleylamine (2 ml) and hexane (20 ml) at room temperature. This precursor mixture was purged under flowing N_2 for ~ 10 minutes. Tert-butylamine borane complex (1 mmol) was dissolved in oleylamine (2 ml) and hexane (2 ml) in a glove box. Then, this reducing solution was quickly injected to the precursor solution in the three-neck flask. The reduction reaction started instantaneously and the color of the precursor solution changed to a deep purple within a few seconds. This solution was stirred for 1 hour at room temperature. Ethanol was then added to the colloidal solution in order to precipitate the Au nanoparticles followed by centrifugation for 20 minutes at 3000 rpm to collect the Au nanoparticles. 60 mg of precipitate (Au nanoparticles) were re-dispersed in 5 ml of hexane. Our primary modification of Peng's recipe involves replacing tetralin with hexane, since tetralin was difficult to fully rinse from the sample and seemed to block surface access during photocatalytic studies.

2.3 Synthesis of Au-ZnO heterostructures

Synthesis of Au-ZnO heterostructures was completed using a previously reported recipe which had been modified to reduce the use of heavier organic solvents that tend to leave surface residue on the samples.[4] Zinc acetate dihydrate (275 mg) was added to a mixture of oleylamine (1.5 ml) and dodecanol (6 ml) in a three-neck flask which was then purged for 10 minutes under N_2 flow. After that, pre-prepared Au seeds (60 mg dispersed in 5 ml hexane) were quickly injected into the flask and the temperature was slowly increased to and held at 140 °C for 90 minuntes. The sample was then allowed to cool to room temperature. The cooled solution was rinsed with an excess of methanol several times, centrifuged, and then rinsed with acetone, centrifuged, and dispersed in hexane. After removing the liquid phase, acetone was added to the test tubes and centrifuged for 10 minutes. The precipitate was dissolved in a small amount of hexane and combined to one test tube. Then, methanol was added to the solution and centrifuged for 10 minutes. This last step was repeated one more time. The precipitate was dried under N_2 flow for few minutes. At this stage, precipitate was no longer soluble in hexane due to the lack of organic capping molecules for solubility. Then, the sample was further cleaned with oxygen plasma for 60 minutes to remove any excess organic molecules.

The pure ZnO nanoparticles were synthesized using the exact same procedure described above for the Au-ZnO heterostructures, except the Au seeds were omitted. Au-SiO_2 was prepared as a control catalyst by mixing 60 mg of Au seeds with 275 mg of commercial SiO_2.

2.4 Characterization of Au-ZnO heterostructures and pure ZnO

An Agilent 8453 UV/Vis/NIR Spectrophotometer was used for all UV-Vis absorption measurements. A March PX-250 Plasma asher was used for O_2 plasma cleaning with an RF power of 100 W and an O_2 pressure of 300 mTorr. A JEOL JEM-2100 Transmission Electron Microscope (TEM) operating at 200 keV was used for both conventional and High Resolution Transmission Electron Microscopy (HRTEM) images of Au-ZnO and pure ZnO samples. A PANalytical powder X-Ray diffractrometer was used to investigate the crystal structure of samples and was operated at 200 kV and 40 mA. The step size of the XRD patterns was 0.016° and the collection time per step was 400 s. The HighScore Plus software package was used for Rietveld refinement.

2.5 Methylene blue degradation reactions

Prior to dye degradation runs the catalysts were treated with an O_2 plasma for ~ 60 mins to remove surface-bound organics from the synthesis steps that could interfere with surface adsoprtion and photocatlytic activity. The FTIR spectra before and after the plasma etching for pure ZnO and Au-ZnO, respectively, illustrate the complete removal of organics (Figure S1).

Methylene blue (MB) dye photodegradation was used as a model reaction in order to investigate the catalytic performance of Au-ZnO. The catalyst (27 mg) was placed into 10 ml of 20 μmol/L MB and soaked overnight (~15 hours) in the dark to stabilize the surface adsorption and desorption equilibrium of the dye. A Newport 300 W Xe arc lamp with a manual shutter was used to illuminate the sample. Agilent 8453 UV/Vis/NIR spectrophotometer was used to collect the absorption spectra during the MB degradation reactions. Edmunds TECHSPEC longpass filters were used for wavelength dependent experiments. In photocatalysis studies, the sample mixture above was exposed to light for 10 mins. Then 6 ml of the reaction solution was centrifuged to separate the solid catalyst from solution. The optical spectrum of the centrifuged solution was then taken. Absorption spectra were recorded every 10 minutes for a total of ~80 minutes. The spectral area under the absorption peak around 664 nm which is the characteristic peak for MB was calculated after the correction of baseline shift and background subtraction to get an accurate estimation for MB concentration. Reproducibility of kinetic parameters determined from dye degradation runs is within approximately 10% and control experiments were conducted to confirm catalytic activity (see results).

3.0 Results and Discussion

3.1 Characterization of nanoparticle samples using UV-Vis absorption spectra

Fig. 1 shows the UV-Vis absorption spectra for the Au seeds, pure ZnO, and Au-ZnO heterostructures used in this study. The broad absorption peak around 510 nm for the Au seeds is due to the plasmon resonance of these nanoparticles. After growth of the ZnO on the seeds, this plasmon resonance red-shifts and narrows due to Ostwald ripening of the Au nanoparticles which occurs at the temperatures used for the growth of ZnO.[4] The changing dielectric environment caused by the newly formed Au-ZnO interface is an additional physical mechanism that likely contributes to the red-shifting of the plasmon feature.[13, 14] To confirm this mechanism we have conducted a simple model calculation (Figure S2) using the quasi-static approximation to estimate the plasmon peak positions and expected shift due to differences in the dielectric environment. Our model calculation predicts that 5 nm Au seeds in hexane have a plasmon resonance at ~504 nm that shifts by ~48 nm when fully encapsulated in ZnO. Considering that our Au particles are slightly larger than 5 nm, have a distribution in sizes, and are not fully encapsulated by ZnO, the resonance features and red-shift noted in Figure 1 are reasonable and qualitatively consistent with a shift due to dielectric changes. Additionally, Khan *et al*[15] have attributed the red-shift noted above, in part, to electron density changes which occur when charge flows from Ag to ZnO as Fermi levels equilibrate. A similar electron density change in Au-ZnO would also cause red-shifting of the plasmon resonance, although quantifying this effect relative to the spectral changes mentioned above is difficult.

Tauc plots of the absorbance spectra (Fig. S3) estimate a direct band gap of ~383 nm (3.23 eV) in the Au-ZnO sample. Comparable optical spectra and bandgap estimates were reported by Peng *et al.*[16] for Au-ZnO heterostructures synthesized in a similar fashion as our study. There is an extremely strong scattering contribution to the pure ZnO spectra between ~380-700nm in Fig. 1 that complicates using Tauc plots and optical measurements for estimating band gaps. We point out that He *et al.*[3] have also reported optical spectra for ZnO nanoparticles with strong scattering contributions.

3.2 Characterization of TEM and HRTEM images

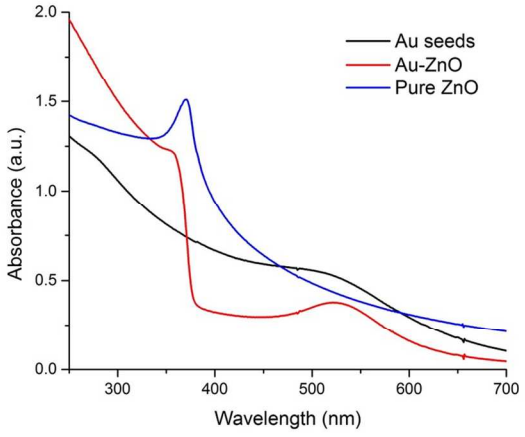

Fig. 1 UV-Vis absorption spectra for Au seeds (black), pure ZnO (blue) and Au-ZnO heterostructures (red).

Pure ZnO was synthesized without the use of Au seeds. In these samples the ZnO has particle sizes of ~20-30 nm (Fig. 2a). The average size of the Au seeds used to nucleate the growth of ZnO is between 4-6 nm (Fig. S4). Representative TEM images of the Au-ZnO heterostructures find Au sizes between 5-7 nm (Fig. 2b). The increase in Au particle size in the heterostructure is consistent with the red-shifted plasmon feature noted in Figure 1. Au nanoparticles that are unattached to ZnO can also be seen in Fig. 2b with diameters of ~ 8-9 nm. These large Au nanoparticles also likely contribute to the red-shifting of the Au plasmon resonance peak. As a result of the free Au seeds, the photocatalysis experiments described below also evaluated similar Au nanoparticles deposited on an inert

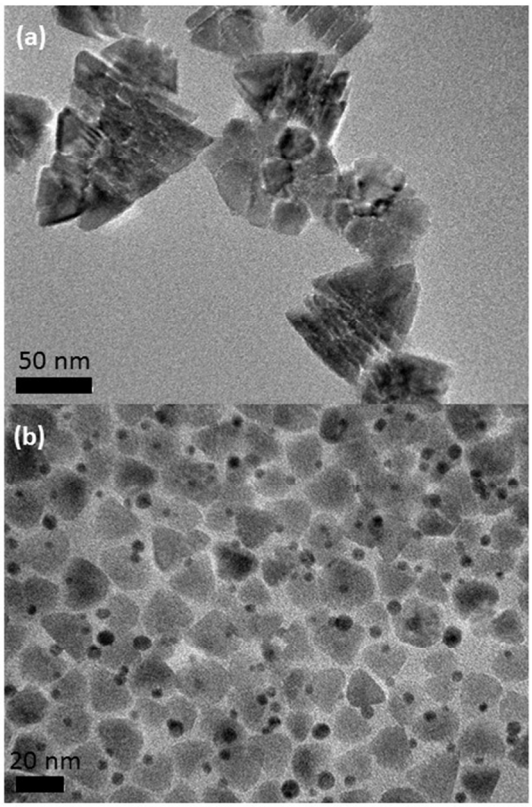

Fig. 2 TEM images of **(a)** pure ZnO and **(b)** Au-ZnO heterostructures.

SiO_2 in order to assess their contribution (or lack of) to the photodegradation of methylene blue (see photocatalysis discussion below).

The TEM images in Fig. 2b show that the ZnO particle sizes in the heterostructures are around 18-22 nm. Additional HRTEM images (Figs. 3 and 4) illustrate the ZnO is single-crystalline and possesses a pyramidal-type morphology with a hexagonally shaped base. A similar nanopyramid shape has been reported previously for the ZnO component of Au-ZnO heterostructures, which are grown using a similar synthetic procedure as we report here.[4] Likewise, similar nanopyramids resulted from a one-pot strategy capable of depositing the Au either at the base

or tips of the pyramids.[1] This type of nanopyramidal ZnO was also reported in a study that synthesized the ZnO structures first and later photodeposited Au particles at the tips.[8] We attribute the more heterogeneous nature of the nanopyramids in our study to the lower levels of surfactants employed for both the Au seed and ZnO synthesis. Organic contamination can interfere with subsequent catalysis studies by blocking access to surface sites and we have minimized their use as much as possible.

The HRTEM images in Fig. 3 provide additional insight on the microstructure of the Au-ZnO samples. The ZnO component of the heterostructure is single-crystalline with ZnO (002) lattice fringes observed. The Au can be identified as polycrystalline particles with multiple Au (111) facets observed having domain sizes of ~ 2.6 nm. This value agrees with the Au (111) domain size of 2.7 nm from the Rietveld analysis (discussed below). The large number of Au (111) facets minimize the surface energy and strain due to the formation of twinned defects.[17] The ZnO (002) plane appears to be parallel to the Au (111) plane at the interface. The basal surface of the ZnO structure is perpendicular to the ZnO (002) direction and the HRTEM images suggest the ZnO crystal starts growing in the [0001] direction, along the *c*-axis, on top of the Au seed. This growth mechanism was proposed by Flomin *et al.*[1] using TEM images of aliquots obtained during different stages of the synthesis.

Interestingly, the *d*-spacing corresponding to the ZnO (002) plane experiences a ~ 3.5% expansion relative to the bulk value of 2.60 Å. This expansion has not been well documented in previous studies of Au-ZnO made by similar synthetic approaches.[1, 4] This expansion only occurs within ~1.5 nm of the ZnO interface with Au (additional analysis details are in the ESI). This lattice expansion gradually decreases and completely disappears ~ 4.5 nm away from the interface where the spacing approaches a constant bulk value of 2.60 Å (Figs. 3, S6, S7, S8 and S9). The plain ZnO nanoparticles do not experience any measurable lattice expansion relative to bulk values (not shown). For comparison, we point out that Shim *et. al.*[18] have previously reported ~1% lattice contraction in CdTe near the CdSe interface of linear barbell heterostructures. The lattice spacing of the CdTe tips on these barbells then approaches bulk values further away from the interface.

TEM images of the Au-ZnO heterostructures also suggest there is variation in the general position of the Au on the basal surface of the ZnO nanopyramid, which is shown in both the images and schematic of Fig. 4. This variation has not been noted in previous structural characterizations of this interface [1, 4, 8] and may result from the changes in surfactants used in the synthesis reported here. In general, it appears that the Au particle does not strictly occupy a position at the center of the ZnO basal plane and can instead occupy a variety of positions. Currently, the role of this structural detail on the photophysics of these samples is not understood.

3.3 X-ray diffraction of nanoparticle samples

Powder XRD patterns confirm the cubic structure of Au nanoparticles and hexagonal wurtzite structure of ZnO (Fig. 5). Rietveld analysis is performed to evaluate crystal size and

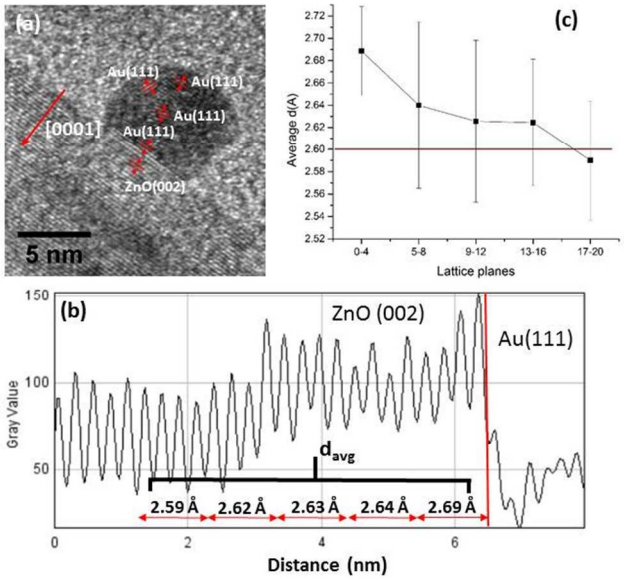

Fig. 3 (a) HRTEM image of the Au-ZnO interface. **(b)** Line scan along the Au-ZnO interface with average lattice spacings for the ZnO (002) plane in the regions shown. **(c)** Average *d*-spacing of ZnO (002) at different distances from the interface. Error bars were determined by analysing 9 different structures.

microstrain in both pure ZnO and Au-ZnO (Figs. S10 and S11). While particle size determinations from a Rietveld analysis of XRD lineshapes are simple to interpret, the precise origin of microstrain contributions to linewidths is more challenging to attribute to a single structural feature.[19-21] The microstrain value determined in a Rietveld analysis is interpreted as a generic deviation from the ideal lattice which can be caused by a variety of crystal-level defects, such as dislocations, domain boundaries, and the expansion/contraction of a lattice. As such, microstrain analysis can provide verification of and insight into some of the microstructure and defects noted in the TEM images above.

The calculated Au particle size in the heterostructure is 2.7 nm, which is consistent with the polycrystalline nature of the Au particles and the (111) domain sizes noted in Fig. 3. The calculated particle size for the pure ZnO sample is 25.9 nm, which is consistent with the TEM images of Figure 2a. The calculated ZnO particle size in Au-ZnO is 20.5 nm which also agrees well with the size determined from TEM images (Figure 2b).

The Rietveld analysis estimates a 0.324 % microstrain for the Au in Au-ZnO which provides evidence for the distribution of Au(111) domains noted in Figure 3. Microstrain estimates for pure ZnO were 0.047 %. The calculated microstrain for the ZnO in the Au-ZnO sample is 0.146 %, which is 3 times larger

than that for pure ZnO. In comparison, Khusaimi *et al.*[22] previously reported a 0.257 % microstrain of ZnO in Au/ZnO heterostructures on a Si substrate.

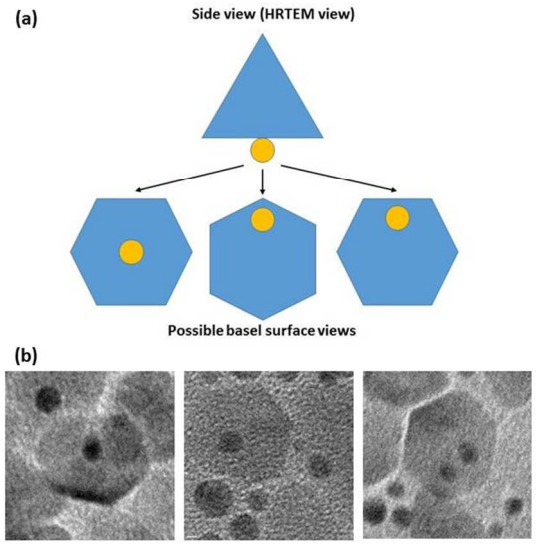

Fig. 4 (a) Schematic diagram for possible orientations of Au nanoparticles on the basal surface of the ZnO nanopyramid **(b)** TEM images of different basal surfaces of the ZnO nanopyramids.

We attribute the increased microstrain for ZnO in the heterostructures to the lattice expansion noted in Fig. 3. The XRD measurement is a bulk probe and averages this defect over the entire sample, including regions where ZnO retains its normal lattice, which likely reduces the magnitude of the microstrain estimate. In fact, we point out that the average lattice expansion in Fig. 3 using the entire ZnO portion of the image (interface and non-interface regions) is only ~0.38 %, compared to ~3.5% at the interface, which illustrates how easily the structural characteristics of the interface can be averaged out.

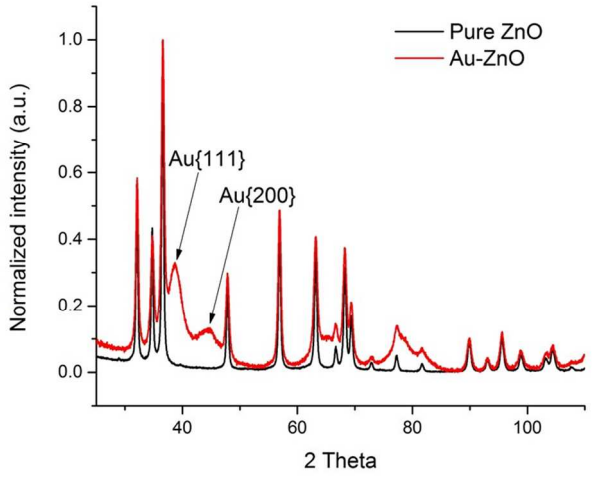

Fig. 5 Comparison of X-ray diffraction patterns of pure ZnO and Au-ZnO core-shell nanoparticles.

3.4 Photocatalytic performance

Fig. 6a shows representative UV-Vis absorption spectra used to determine the kinetics of MB photodegradation under $\lambda > 295$ nm irradiation. Fig. 6b shows photodegradation kinetics for pure ZnO, Au-ZnO, Au-SiO_2 and a stock solution of 20 μmol/L MB (no catalyst) also at $\lambda > 295$ nm. After 60 minutes of illumination, Au-ZnO photodegrades ~98 % of the MB. In comparison, pure ZnO only degrades ~17 %, the Au/SiO_2 control ~ 4 %, and the stock solution of MB (without catalyst) ~10 %. Plots of $\ln(C/C_0)$ versus time are linear (Fig. S12) which confirm the pseudo first order reaction kinetics and associated degradation mechanisms noted in many MB photodecomposition studies.[14] The exceptional activity for Au-ZnO combined with the low or lack of activity for ZnO, Au-SiO_2 and MB alone, point to the synergistic role of the Au and ZnO in the heterostructured materials.

Wavelength dependent photodecomposition studies were employed to help answer mechanistic questions about the photophysics of these samples. Fig. 6c shows photodegradation kinetics of MB using $\lambda > 295$ nm, $\lambda > 320$ nm and $\lambda > 400$ nm longpass filters. Fig. 6d, illustrates that the catalytic activity of Au-ZnO remains almost constant between 295 nm $< \lambda <$ 320 nm. But for $\lambda > 400$ nm, Au-ZnO has no appreciable activity. The calculated pseudo first order rate constants of Au-ZnO were 0.063 min^{-1}, 0.071 min^{-1} and 0.003 min^{-1} for $\lambda > 295$ nm, $\lambda > 320$ nm and $\lambda > 400$ nm illumination, respectively. This confirms the necessity of direct bandgap excitation of ZnO in the Au-ZnO heterostructure (bandgap ~ 383 nm, Figure S12) in order to initiate the photodecomposition of MB. P25 TiO_2 has comparable kinetics for MB degradation (Figure 6d) for $\lambda >$ 295 nm, but this activity approaches zero for $\lambda > 320$ nm. P25 TiO_2 has a comparable bandgap to ZnO and we suspect that the large difference in activity towards MB results, in part, from the lack of metal co-catalysts on the TiO_2 sample for shuttling electrons into solution. In addition, the Au-ZnO heterostructures have subtle changes in electronic structure and band alignments (discussed below) that also likely contribute to their improved activity over P25 TiO_2.

Several previous works have reported higher catalytic activity of Au-ZnO heterostructures over pure ZnO using dye degradation reactions.[1-8, 14, 23-26] Direct comparisons of these efforts and our own are difficult due to different reaction conditions and dyes used. One reasonable method for comparing these works involves evaluating the differences in % decomposition between the ZnO and Au-ZnO catalysts. Yao *et al.*[8] showed that methyl orange decomposition was ~ 1.5 times faster with Au-ZnO over ZnO. Li *et al.*[4] and Wang *et al.*[7] showed that rhodamine B decomposition was ~2 times faster with Au-ZnO versus ZnO. Lee *et al.*[23] showed that the degradation of rhodamine 6G was ~3 times faster with Au-ZnO over ZnO. In our current work, the degradation of methylene blue was ~6 times faster with Au-ZnO than pure ZnO.

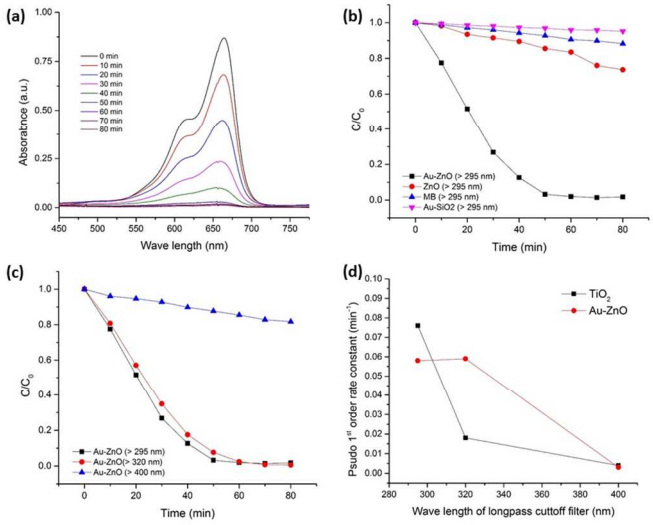

Fig. 6 (a) UV-Vis absorption spectra for MB degradation using Au-ZnO with $\lambda > 295$ nm **(b)** MB degradation results for Au-ZnO (black), ZnO (red), MB solution (no catalyst) (blue) and Au-SiO_2 (magenta) with $\lambda > 295$ nm illumination **(c)** Wavelength dependent MB degradation with Au-ZnO **(d)** Pseudo first order rate constants for MB degradation with Au-ZnO and TiO_2 using different longpass filters.

It is interesting to analyse reasons for the enhanced photocatalytic activity of Au-ZnO over ZnO. Plasmonic heating,[27] direct electron injection[10] from Au, and field-enhancement created by Au plasmon resonance[28], can all be easily ruled out from the wavelength dependent studies of Fig. 6c. If the Au plasmon was playing a critical role in the photophysics of this sample, one would expect to see photocatalytic activity at wavelengths longer than 400 nm. The loss of activity towards MB as the irradiation wavelength becomes sub-bandgap clearly points to a mechanism where direct gap excitation generates charge carriers that eventually create the radical species in solution that degrade MB. We also point out that the lack of catalytic activity seen for Au nanoparticles on SiO_2 (Figure 6b) helps to rule out any potential mechanisms involving interband transitions from occupied *d*-bands below the Fermi level (E_f) to unoccupied *s-p* bands above the E_f of Au, as was observed experimentally by Cronin *et al.* for the photocatalytic reduction of CO_2 with Au/TiO_2[28].

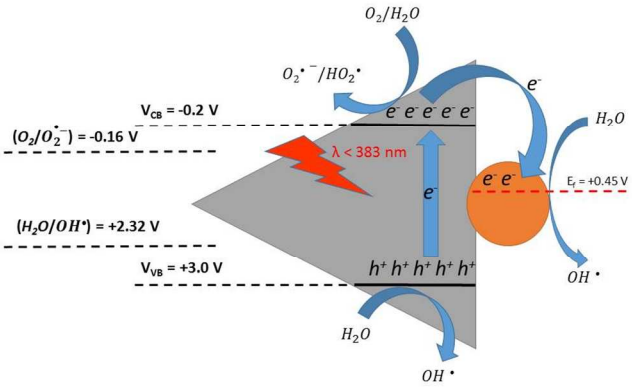

Fig. 7 Approximate band alignment of Au-ZnO. Potentials are with respect to NHE.

The characterization and photocatalytic activity data presented above allow us to propose how Au enhances the photoactivity of the heterostructures towards MB degradation (Figure 7). Direct gap excitation creates electrons and holes, which thermalize to the bottom and top of the conduction and valence bands, respectively, of ZnO. The energy of the conduction band minimum and that of the valence band maximum of ZnO are −0.2 eV and +3.0 eV respectively, with respect to the Normal Hydrogen Electrode (NHE).[29] The Fermi level of Au is +0.45 eV with respect to NHE.[3] Since the Fermi level of Au is below the conduction band of ZnO, the photoexcited electrons are easily transferred to the Au nanoparticles from the conduction band of ZnO.[7] The close contact of the ZnO and Au nanoparticles increases this charge separation efficiency helping to reduce carrier recombination.[3] The build-up of electrons in Au will shift E_f in a more negative direction but the electron transfer from ZnO to Au would not be altered until E_f approaches the conduction band minimum of ZnO. The electrons at the E_f of Au can be injected into H_2O species to form $OH^{\bullet}$ radicals. The charge separation described above also facilitates injection of the hole left behind in the valence band into water to generate $OH^{\bullet}$ radicals, which attack MB directly and contribute to the photodegradation. The products observed from this photodegradation mechanism of MB have been identified in previous works as CO_2 gas, nitrate, sulfate and ammonium.[30]

In addition to charge separation, the Au in heterostructures is known to decrease the work function of a metal oxide, which can impact carrier generation and injection.[9] Sykes *et al.*[9] have demonstrated that the work function of TiO_2 can decrease from 5.3 eV to 4.8 eV with increasing Au loading due to an interfacial dipole created as charge flows from Au to TiO_2 in order to equilibrate Fermi levels. The work function of ZnO and that of Au are 5.3 eV and 5.1 eV, respectively, which indicates a similar mechanism could occur with these heterostructures.[31, 32] The lowered ZnO work function caused by equilibration with the Au Fermi level would increase the transfer rate of conduction band electrons from the ZnO surface

to adsorbed O_2 (rate limiting step of the photocatalytic MB degradation) and H_2O to form $O_2^{\bullet}$ and $HO_2^{\bullet}$ radicals, respectively.[6, 7, 33, 34]

4.0 Conclusions

Au-ZnO heterostructures were synthesized using a literature recipe that has been modified to reduce the amount of organic surfactants. The resulting Au-ZnO heterostructures have a nanopyramid geometry composed of ZnO with Au nanoparticles attached to the basal surface. The (002) planes of ZnO expand by ~3.5% in the first ~1.5 nm of the interface and approach bulk values of 2.60 Å towards the apex of the nanopyramid. The band gap of the Au-ZnO heterostructures is estimated to be 388 nm (3.23 eV). Wavelength dependent photodecomposition studies with methylene blue indicate that direct gap excitation of the ZnO component of the heterostructure is required to decompose the dye. Au-ZnO heterostructures decompose the dye 6 times faster than simple ZnO. The improved photocatalytic activity of Au-ZnO is largely attributed to the physical separation of photoexcited electrons and holes caused as electrons are injected from the conduction band minimum of ZnO to the Fermi level of Au which leads to facile generation of radicals in solution which decompose the dye. Likewise, we also hypothesize that heterostructuring ZnO with Au can cause a decrease of the work function of ZnO which would also improve lead to improved electron injection from the conduction band to electron acceptors.

Acknowledgements

This technical effort was performed under RES contract DE-FE0004000. This report was prepared as an account of work sponsored by an agency of the United States Government. The U.S. Government is authorized to reproduce and distribute reprints for Government purposes notwithstanding any copyright notation hereon.

Notes and references

* christopher.matranga@netl.doe.gov, Tel: +1-412-386-4114; oranasin@mix.wvu.edu, Tel: +1-304-627-1193
[a] Department of Physics and Astronomy, West Virginia University, Morgantown, WV 26506, United States.
[b] National Energy Technology Laboratory, U.S. Department of Energy, 626 Cochrans Mill Road, Pittsburgh, PA 15236, United States.
[c] URS Corporation, P.O. Box 618, South Park, PA 15129, United States.

Electronic Supplementary Information (ESI) available: Additional electron microscopy images, characterization data, and image/data analysis details. See DOI: 10.1039/b000000x/

1. K. Flomin, I. Jen-La Plante, B. Moshofsky, M. Diab and T. Mokari, *Nanoscale*, 2014, 6, 1335-1339.
2. Z. Han, L. Wei, Z. Zhang, X. Zhang, H. Pan and J. Chen, *Plasmonics*, 2013, 8, 1193-1202.
3. W. He, H.-K. Kim, W. G. Wamer, D. Melka, J. H. Callahan and J.-J. Yin, *J. Am. Chem. Soc.*, 2013, 136, 750-757.
4. P. Li, Z. Wei, T. Wu, Q. Peng and Y. Li, *J. Am. Chem. Soc.*, 2011, 133, 5660-5663.
5. M. Misra, P. Kapur and M. L. Singla, *Appl. Catal., B*, 2014, 150–151, 605-611.
6. C. Mondal, J. Pal, M. Ganguly, A. K. Sinha, J. Jana and T. Pal, *New J. Chem.*, 2014, 38, 2999-3005.
7. Q. Wang, B. Geng and S. Wang, *Environ. Sci. Technol.*, 2009, 43, 8968-8973.
8. K. X. Yao, X. Liu, L. Zhao, H. C. Zeng and Y. Han, *Nanoscale*, 2011, 3, 4195-4200.
9. E. C. H. Sykes, F. J. Williams, M. S. Tikhov and R. M. Lambert, *J. Phys. Chem. B*, 2002, 106, 5390-5394.
10. S. K. Cushing and N. Wu, *Interface*, 2013, 63-67.
11. H. Yu, H. Ming, H. Zhang, H. Li, K. Pan, Y. Liu, F. Wang, J. Gong and Z. Kang, *Mater. Chem. Phys.*, 2012, 137, 113-117.
12. S. Peng, Y. Lee, C. Wang, H. Yin, S. Dai and S. Sun, *Nano Research*, 2008, 1, 229-234.
13. W. Wu, L. Liao, S. Zhang, J. Zhou, X. Xiao, F. Ren, L. Sun, Z. Dai and C. Jiang, *Nanoscale*, 2013, 5, 5628-5636.
14. H. Yin, K. Yu, C. Song, R. Huang and Z. Zhu, *ACS Appl. Mater. Interfaces*, 2014, 6, 14851-14860.
15. M. Khan, C. Wei, M. Chen, J. Tao, N. Huang, Z. Qi and L. Li, *J. Alloys Compd.*, 2014, 612, 306-314.
16. P. Li, D. Wang, Z. Wei, Q. Peng and Y. Li, *Chem. Eur. J.*, 2013, 19, 3735-3740.
17. Z. L. Wang, *J. Phys. Chem. B*, 2000, 104, 1153-1175.
18. M. Shim, H. McDaniel and N. Oh, *J. Phys. Chem. Lett.*, 2011, 2, 2722-2727.
19. M. R. Daymond, M. A. M. Bourke, R. B. VonDreele, B. Clausen and T. Lorentzen, *J. Appl. Phys.*, 1997, 82, 1554-1562.
20. N. C. Popa and D. Balzar, *J. Appl. Crystallogr.*, 2001, 34, 187-195.
21. A. Leineweber, *Zeitschrift Fur Kristallographie*, 2011, 226, 905-923.
22. Z. Khusaimi, M. H. Mamat, N. Abdullah and M. Rusop, *J. Nanomater.*, 2012, 2012, 8.
23. J. Lee, H. S. Shim, M. Lee, J. K. Song and D. Lee, *J. Phys. Chem. Lett.*, 2011, 2, 2840-2845.
24. S. A. Ansari, M. M. Khan, S. Kalathil, A. Nisar, J. Lee and M. H. Cho, *Nanoscale*, 2013, 5, 9238-9246.
25. N. Udawatte, M. Lee, J. Kim and D. Lee, *ACS Appl. Mater. Interfaces*, 2011, 3, 4531-4538.
26. P. Fageria, S. Gangopadhyay and S. Pande, *R. Soc. Chem. Adv.*, 2014, 4, 24962-24972.
27. C. Wang, O. Ranasingha, S. Natesakhawat, P. R. Ohodnicki, M. Andio, J. P. Lewis and C. Matranga, *Nanoscale*, 2013, 5, 6968-6974.
28. W. Hou, W. H. Hung, P. Pavaskar, A. Goeppert, M. Aykol and S. B. Cronin, *ACS Catalysis*, 2011, 1, 929-936.
29. A. J. Nozik and R. Memming, *J. Phys. Chem.*, 1996, 100, 13061-13078.
30. A. Houas, H. Lachheb, M. Ksibi, E. Elaloui, C. Guillard and J.-M. Herrmann, *Appl. Catal., B*, 2001, 31, 145-157.
31. T. Zhai, H. Liu, H. Li, X. Fang, M. Liao, L. Li, H. Zhou, Y. Koide, Y. Bando and D. Golberg, *Adv. Mater.*, 2010, 22, 2547-2552.
32. Z. Zhang, G. Meng, Q. Xu, Y. Hu, Q. Wu and Z. Hu, *J. Phys. Chem. C*, 2009, 114, 189-193.
33. M. Ahmad, S. Yingying, A. Nisar, H. Sun, W. Shen, M. Wei and J. Zhu, *J. Mater. Chem.*, 2011, 21, 7723-7729.
34. X. Hou, *Mater. Lett.*, 2015, 139, 201-204.

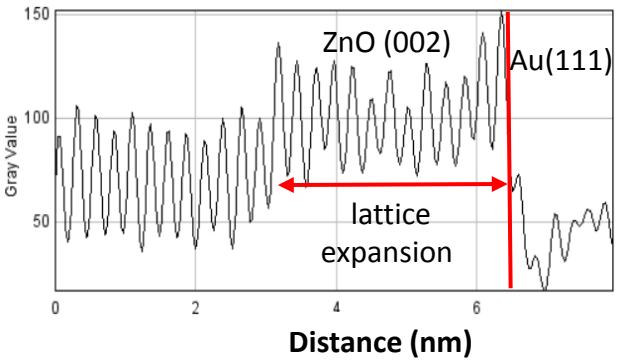

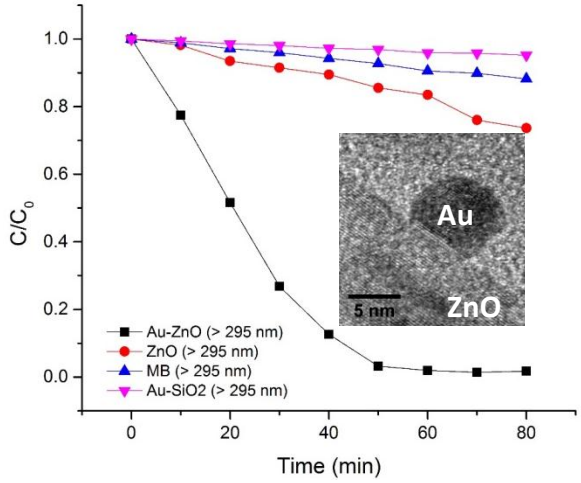

ZnO nanopyramids have been grown on top of Au nanoparticle seeds creating a unique heterostructured system for photocatalytic applications